P-ISSN 2586-9000
E-ISSN 2586-9027
Homepage : https://tci-thaijo.org/index.php/SciTechAsia
Science & Technology Asia
Vol.28 No.2 April - June 2023
Page: [100-111]
Original research article

Investigations on Microstructure, Tensile Properties and Crystallographic Orientation of SAPH440 CMT Weldments

Niwat Mookam[1,*], Ratthasak Prommas[2], Phadungsak Rattanadecho[3], Uraiwan Pongsa[1], Phoometh Sangrayub[1]

[1]*Department of Industrial and Production Engineering, Faculty of Industry and Technology, Rajamangala University of Technology Rattanakosin, Prachuapkhirikhan 77110, Thailand*
[2]*Department of Mechanical Engineering, Faculty of Engineering, Rajamangala University of Technology Rattanakosin, Nakhon Pathom 73120, Thailand*
[3]*Research Center of Microwave Utilization in Engineering, Faculty of Engineering, Thammasat University, Pathum Thani 12120, Thailand*

Received 30 March 2022; Received in revised form 17 December 2022
Accepted 28 December 2022; Available online 14 June 2023

ABSTRACT

In this research, investigations on microstructure, tensile properties and crystallographic orientation were carried out on SAPH 440 steel welded using cold metal transfer (CMT). Comparisons are made between the variables of weld voltage and weld travel speed. Weldments were free from distortion as characteristic of the low heat input from CMT. An optimal condition with excellent surface quality, low defects and high tensile strength was found to be 12 V and 50 mm/min travel speed conditions. The ferrite phase with a body centered cubic crystal structure is presented in the microstructures. Finally, the larger degree of preferred orientation was detected at the {100} plane. In addition, a low recrystallization resulted in low-angle grain boundaries, and higher residual strain in the microstructures was correlated to the high strength of weld seam.

Keywords: CMT; Crystallographic orientation; Defects; EBSD; Tensile strength

1. Introduction

Hot rolled steel is widely used in automobile manufacture because of its excellent press formability, high strength and good weld-ability. According to the SAPH440 steel specification, it is applied to automobile frame and other parts. The microstructure of the steel base mainly consists of uniform grains of ferrite and a small amount of pearlite [1, 2]. Several types of welding methods exist to joint the structure together, each with various pros and cons. Arc welding with higher voltage and larger heat input alters the micro-structure of the weld and near-weld area to become coarser and the corresponding

***Corresponding author:** niwat.moo@rmutr.ac.th
doi: 10.14456/scitechasia.2023.30

hardness gradually decreases [1]. Laser welding can cause a heat affected zone (HAZ) transformation from ferrite to austenite due to the heat generated. In addition, the structure shows a mixture of martensite and ferrite due to rapid cooling [2]. In the case of spot welding, the martensite phase in the fusion zone (FZ) is formed due to the rapid cooling. The larger martensite phase is often a precursor to reduced mechanical performance [3]. Similarly with tungsten inert gas (TIG) welding, a high cooling rate causes extreme hardness and brittleness in the weld zone (WZ) due to a higher proportion of martensite phase [4]. Shielded metal arc welding (SMAW) of low carbon steel found that the FZ and HAZ contains grains larger than those in the base metal and phase transformations that occur in the HAZ during cooling [5]. In the case of high strength steel, the strength of both HAZ and weld metal is higher than that of the parent material due to higher residual stress [6]. However, this may not be the only reason for the higher strength of the HAZ. The welding of mild steel plates with high current and voltage with gas tungsten arc welding (GTAW) shows that the bead width and HAZ also increases with increasing welding current [7]. Thus, high heat input and rapid cooling rate affect the microstructure and degrade some mechanical properties. In addition, the spatters caused by the metallurgical reaction in welding process and unstable arc are unfavorable. The research team of Zhao et al. [8], discovered the occurrence of the reduction of splash quantity with use of a shielding gas; the Ar gas prevents oxidation and suppresses formation of carbon monoxide. A stable arc in welding is more effective in the avoidance of spatter [9].

Cold Metal Transfer (CMT) has benefits of low heat input and good arc stability making it suitable for a wide variety of applications in automobile manufacture [10]. This process has several current and voltage waveforms which depend on the welding operation to be conducted. Typically, a low current and voltage is used for welding. Low heat-input results in lower dilution and finer microstructure resulting in a high hardness of the bead [11]. Nevertheless, the heat input alone cannot be a good criterion to judge the effect of the welding process on the final state of strain in the HAZ, and both welding speed and current should be taken into account. However, the thermal changes can influence the microstructure through several phenomena, such as recrystallization, grain growth, and phase transitions during welding [12, 13]. These processes lead to the formation of a preferred orientation, e.g., grains grow along a certain preferred crystallographic direction, such as with weld metal and the HAZ from ferrite with the BCC structure (110), (200) and (111) [5]. The evolution of low and high angle grain boundaries within a deformed grain affects the mechanical properties, *i.e.* high angle grain boundaries (HAGBs) are playing active role in fatigue fracture [14]. Increased HAGBs are caused by a recrystallized texture in the cold metal transfer [15, 16]. Therefore, it is difficult to determine a clear picture regarding the orientation of the morphologies. Hence, knowledge of the relationships between crystallographic orientation and mechanical properties is valuable, but little information is available in the literature for the welding characteristics. This research is intended to investigate an optimal CMT welding variables of microstructure, tensile strength and crystallographic orientation of SAPH440 steel. A laser profile scan was used to investigate surface and defects of welds. The electron backscatter diffraction (EBSD) techniques were applied to ascertain the crystallographic orientation.

2. Materials and Methods

The material used in the study was SAPH440 steel. The chemical composition

of the steel-substrate was as follows in wt%: C≤0.210, Si≤0.30, Mn≤1.500, S≤0.025, P≤0.025, Al≤0.010 and balance Fe. The substrates were divided into rectangular plates of 100×100×1.5 mm dimensions. The filler wire was ER70-G3/4Si with a diameter of 0.8 mm. The CMT welding machine in this experimental was a Fronius model Trans Pulse Synergic 2700. During welding, pure argon gas 99.99 % was used as shielding gas to protect the molten pool. The contact tip was fixed to the automatic moving machine (Thermatech, TM-12M-1T/2T) to provide a constant welding speed. Two welding parameters were selected for the experiment as follows: voltage settings of 10, 12, 14, and 16 V and weld travel speeds of 25, 50, and 100 mm/min. After welding, visual inspection and the shape of the weld metals was determined by a 3D scanner (GOM, Atos Core 300). All test samples were cut using wire-EDM (Mitsubishi, FA20S Advance) was utilized to prepare the tensile samples. The tensile testing was performed using a universal testing machine (Zwick, Z020).

The specimens for microstructural examination were firstly polished and then etched with an ion mill using a Hitachi, IM 4000 Plus. An Jeol JSM-580LV scanning electron microscope (SEM) was used to verify the microstructure. The chemical composition of the microstructure was determined using the Oxford Instruments X-Max energy dispersive spectroscope (EDS). In addition, the lattice structure of the phases was analyzed using the Bruker AXS D8-Discover X-Ray diffractometer (XRD). The crystallographic orientation was determined by EBSD using a Hitachi SU8230 field emission scanning electron microscope (FE-SEM) equipped with an Oxford EBSD detector.

3. Results and Discussion

3.1 Surface and defects

The welded metal comparison between the original weld seam and 3D scan of the entire weld seam is shown in Fig. 1. The results show that there is a difference in the uniformity of weld pool. There was a great difference with non-continuous beads in the final length of the weld pool as shown in Fig. 1(a). The differences were directly related to the impact of electrical explosion at the end of the short circuit [17]. Moreover, deposition of the weld pool is found to be non-continuous with several settings with the occurrence of spattering. This was due to lower metal transfer stability with voltage condition and high travel speed which led to a higher spattering production. It was observed that the most complete and uniform surface of welds occurs at the travel speed of 50 mm/min, with position measurements in the range of 10-90 mm (in Fig. 1(b)), in comparison to the other travel speeds. In addition, the surface substrate had minimal spatter formation. That means high transfer stability led to low spatter formation. A larger voltage and high travel speed led to a higher spattering production and non-continuous weld pool as shown in Fig. 1(c), indicating there is a lower metal transfer stability with higher travel speeds in the welding processes. However, no distortion or undercut defects were found and straightness was good for all weld beads.

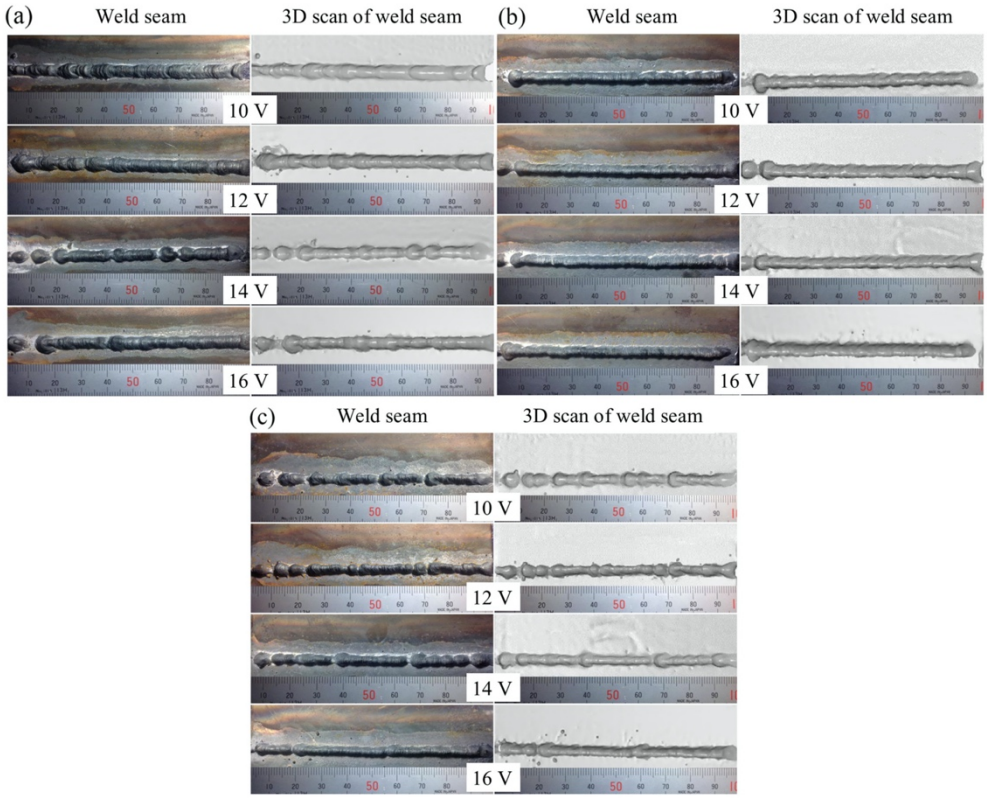

Fig. 1. Weld seam and 3D scan of weld bead; (a) 25 mm/min, (b) 50 mm/min, and (c) 100 mm/min.

The bead width of weld seams are shown in Fig. 2. As the voltage increased from 10-14 V, the bead width was decreased. When the excitation voltage was 16 A with the travel speed of 50-100 mm/min, the bead width kept constant. Lin et al. [18], report the bead width constant with increasing current of MIG due to some droplets not dropping into the weld pool, which caused elevated spattering. The maximum bead width reached 5.260 mm (10 V, 25 mm/min) and the minimum was 3.045 mm (16 V, 100 mm/min). Fig. 3, presents the bead height from various welding conditions. In the case of the 25 and 50 mm/min speeds, the weld bead height followed a bell curve peaking between 12 and 14 V. Increasing the travel speed to 100 mm/min reduces the bead height in comparison to slower speeds, and the bell curve changes to a parabola form. Because of the enhanced travel speed and lower heat input with 10 and 12 V the deposition of weld pool is found to be non-continuous, a more uniform and complete surface of weld is deposited at the higher voltages as shown in Fig. 1(c).

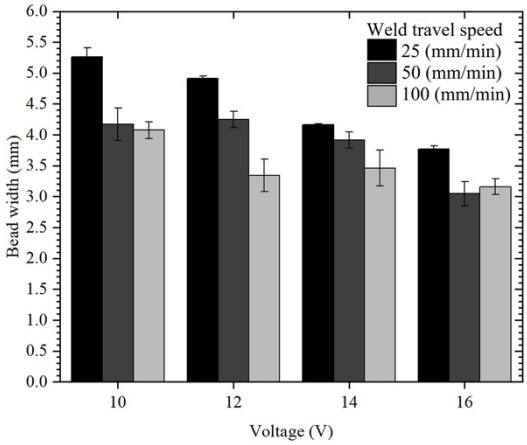

Fig. 2. Bead width of weld seam.

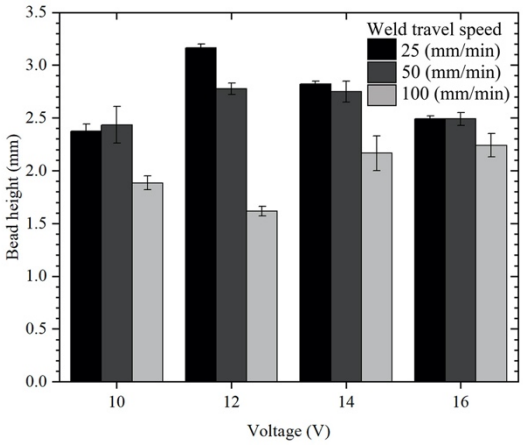

Fig. 3. Bead height of weld seam.

The average maximum and minimum values of bead height at 12 V were 3.165 and 1.615 mm, for 25 mm/min and 100 mm/min, respectively. The heat input is directly proportional to the arc voltage and inversely proportional to the welding speed [19]. An increase in the spreading of filler wire on the substrate could be attributed to the increased heat input. However, the situation is reversed if increasing the speed. The bead height of the weld seam was minimally increased for the weld travel speed of 100 mm/min. SEM was used to examine the microstructure of the weld zone as shown in Figs. 4-6. The result indicated that porosity defects occurred. The formation of the porosity was contained within the FZ and fusion line. The presence of large porosities near the fusion line of weld beads were found. An absence of porosity is desirable for a more reliable weld seam. In this research, despite the presence of some porosity in all conditions, the lowest porosity occurred at a current condition of 12 V and a speed of 50 mm/mm, probably due to the better stability of the arc. In addition, the dilution of the bead occurred appropriately for this condition. The conventional rule of increasing dilution with increasing heat input does not hold well in CMT [11]. Thus, the dilution was close to zero under the influence of welding with an unstable arc.

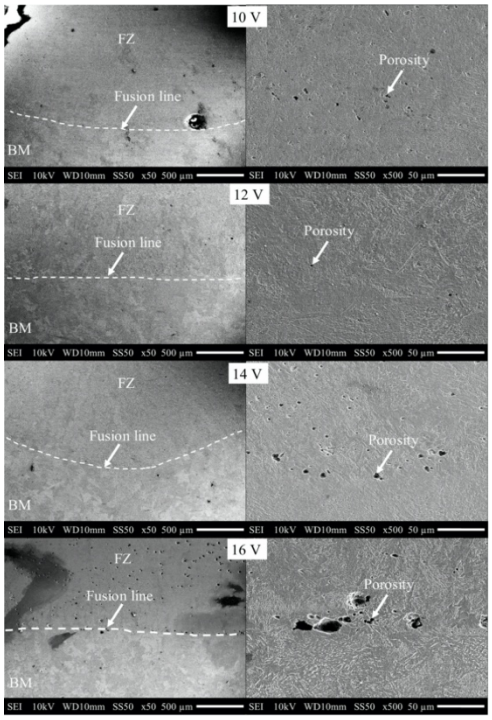

Fig. 4. SEM microstructure and porosity in weld seam, 25 mm/min.

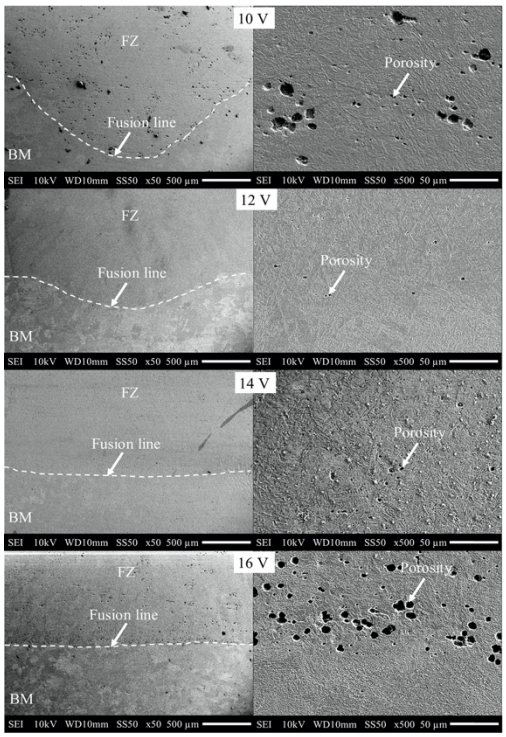

Fig. 5. SEM microstructure and porosity in weld seam, 50 mm/min.

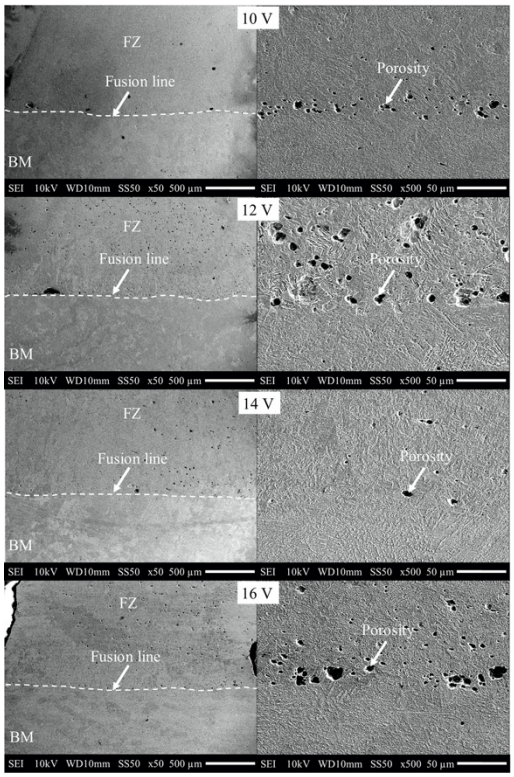

Fig. 6. SEM microstructure and porosity in weld seam, 100 mm/min.

3.2 Tensile strength

The tensile strength of the weld seam for all experiments is shown in Fig. 7. The tensile strength of low voltage (10 and 12 V) also depended on the voltage and travel speed variables. As the travel speed of the welding increased, the tensile strength of the weld seam decreased. Moreover, the poor tensile strength of the weld seam due to the faster travel speeds is due to instability of the melt transfer when the feed increases [20]. A more non-uniform bead i.e., low bead width and low penetration depth, results in less strength. The tensile strength of 12 V was higher than that of 10 V. Thus, in this condition the increase in the strength of sample could be attributed to the increased heat input in welding processes. The higher heat input leads to higher penetration depth due to a higher temperature in the melt pool [21]. However, under the higher voltage conditions of 14 V and 16 V, the tensile strength was not dependent on the voltage and travel speed because of instability in the addition of filler metal to the weld zone. This causes the tensile strength effect to be inconsistent in this condition. However, the weld seams exhibited significantly better tensile strength than the steel substrate. The tensile strength was 5191.05 N for the steel substrate.

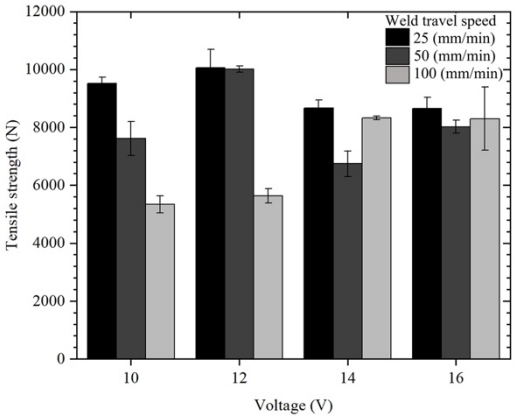

Fig. 7. Tensile strength of weld seam.

In terms of optimal tensile strength, it was found that the 12 V weld was best, with a difference of less than 1.0% of tensile force between 25 and 50 mm/min travel speed. Thus, given the low porosity and good uniformity, the optimal welding conditions were chosen to be 12 V and 50 mm/min travel speed. This weld seam has high surface quality, a uniform and continuous weld pool, few defects and does not have oversized weld bead geometry.

3.3 Microstructure and crystallographic orientation

The optimal conditions in the term of high strength according to the results in Fig. 7, occurred at 12 V with a travel speed of 50 mm/min and poorly parameters appeared at 10 V with a travel speed of 100 mm/min, respectively. FE-SEM and EBSD were used to analyze the microstructure and orientations in the weld zone *e.g.,* weld metal (WM) and base metal (BM). The microstructure and EBSD scans were an

area of 500×500 µm shown in Fig. 8. The dotted line separates WM (Top) and BM (Bottom). In addition, the dash-dotted curve shows the deep penetration welding to improve the tensile strength.

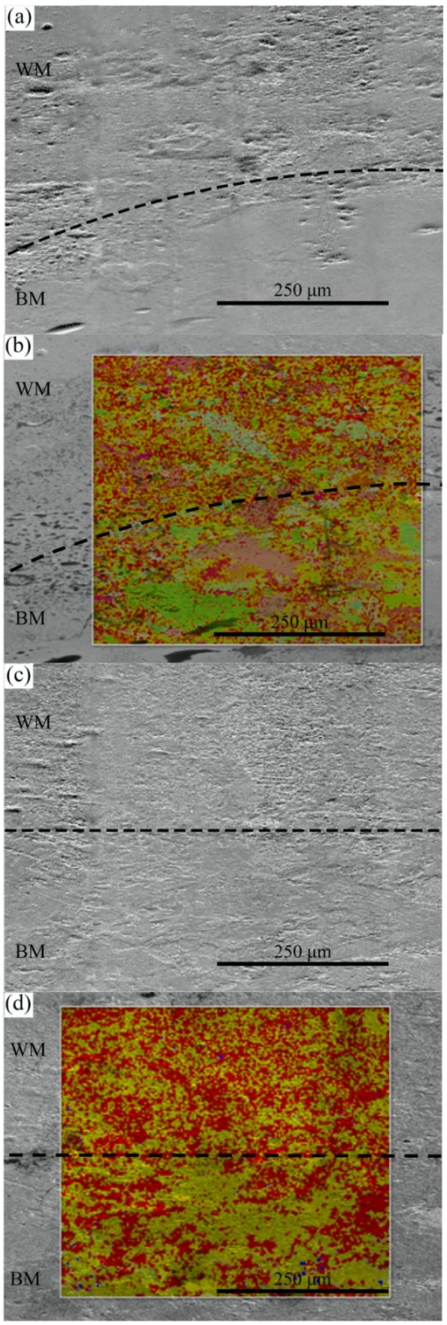

Fig. 8. Fe-SEM and EBSD scans of weld seam; (a)-(b) high strength and (c)-(d) low strength.

Fig. 9 illustrates the EDS analysis of the weld seam. The results show the higher iron-Fe in the weld seam. The XRD spectrum indicated the presence only of the ferrite phase as shown in Fig. 10. The lattice parameters of ferrite phase were 0.286080 nm. In addition, the ferrite phase conforms to a BCC structure and a space group of Im-3m (229). The diffracted peaks of ferrite phase are found at 44.67, 64.93, and 82.50 degrees, which corresponds to crystallographic diffraction peaks of (110), (200), and (211), respectively. The phase formation findings in this study are consistent with Boumerzoug et al. [5], who documented that the ferrite phase occurred in weld metal and HAZ of low carbon steel, with the maximum intensity of the peak approximately 44.00 degrees. Among difference welded methode affect on maximum intensity of the peak and grain size in the metal and HAZ, due to the heat being applied during welding process [22].

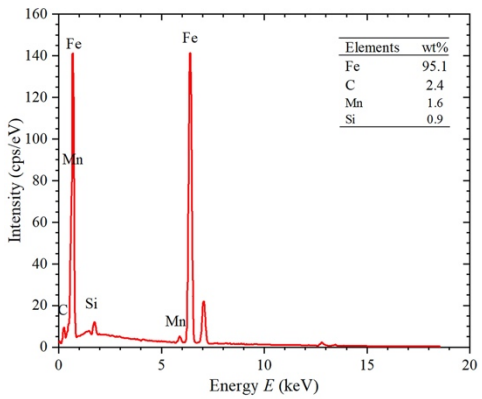

Fig. 9. EDS analyses patterns of weld seam.

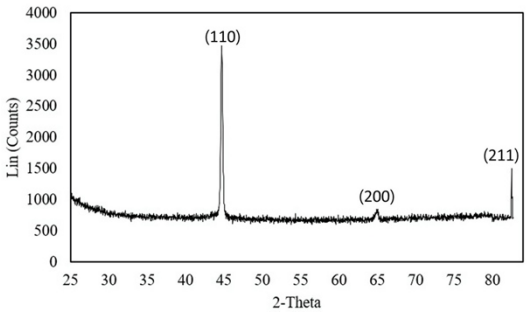

Fig. 10. The XRD patterns of weld seam.

The grain orientations of each of the EBSD test samples is shown in Fig. 11. In IPF maps, the crystallographic orientation for each individual point is shown by the colour pixels attributed to the (hkl) planes, whereby red is representative of (001), green (101), and blue (111).

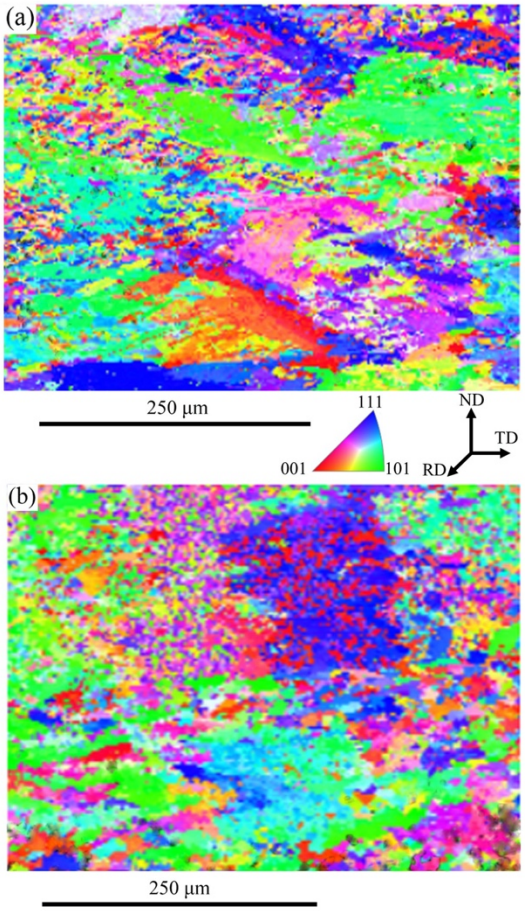

Fig. 11. IPF of the grains in weld seam; (a) high strength and (b) low strength.

The crystallographic orientation is defined by a crystalline reference local frame in three orthogonal directions: rolling direction (RD), natural direction (ND) and transverse direction (TD). Here in samples, the RD plane is the cross-section of the weld and ND plane is the surface of the weld. By comparison, the grain size of the high strength sample (Fig. 11(a)) was larger than that of the low strength sample (Fig. 11(b)). Especially, the green region with (101) plane at the boundary region forms larger islands. This was due to the low welding speed which led to larger heat input during welding processes [23]. The deformation capacity of the equiaxed grain zone is a key factor to the tensile strength, consistent with Yu et al. [24], who reported that the tensile strength and elongation increase with increasing width of equiaxed grain zone.

Fig. 12 gives the PF of ferrite phase in the weld seam, with respect to the weldment where TD and ND refer to the x and y axes, respectively. The crystallographic texture of the two samples also showed some considerable differences. The multiples of uniform distribution or MUD also reflected the different levels of deformation, and the larger MUD value indicates more deformation. The experimental results indicate that the crystallographic texture or deformation (higher MUD) is formed on the {100} plane. It could be observed that red regions of the low strength sample show the spread of the non-uniform distribution and were found for both {100} and {111} planes. The mean maximum orientation spread (MOS), represents the value of the maximum angular misorientation from the mean orientation within grains. MOS values and distribution of the iron-Fe matrix phases in each weld seam are shown Fig. 13. It shows a high frequency of phase, but MOS occurs at some position with high MOS value. In the work of Ifergane et al. [25], the misorientation analyses revealed that in the deformed regions, the frequency of very low-angle (1-2°) misorientation dramatically decreased as the deformation was increased, indicating a sub-grained structure and dislocation activity.

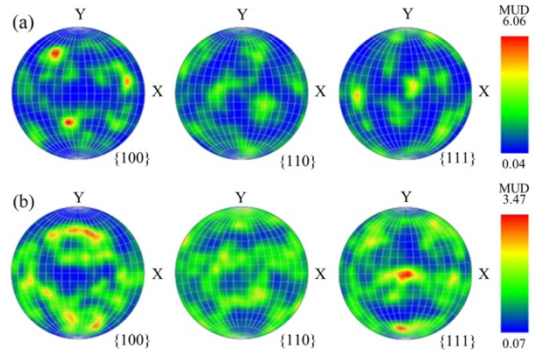

Fig. 12. PF of the Fe matrix phases in weld seam; (a) high strength and (b) low strength.

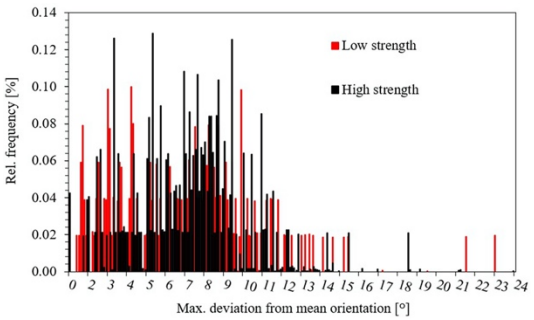

Fig. 13. MOS in weld seam.

Three types of microstructures are identified and shown in Fig. 14 as deformed, sub-structured, and recrystallized structures, marked by red, yellow and blue, respectively. The deformed behaviors were similar for both samples; the low strength sample was more recrystallized than that the high strength sample. A significant transition from the deformed mechanism to the recrystallized mechanism by weld travel speed is found in the low strength sample. Thus, the larger recrystallized microstructure and distribution result in lower tensile force of the weld bead. Recovery and recrystallization occur in the microstructure and leads to the reduction in the magnitude of strain stored in the grains [26]. In addition, the deformed grains consume the stored strain energy as evident in the reduction of LAGBs.

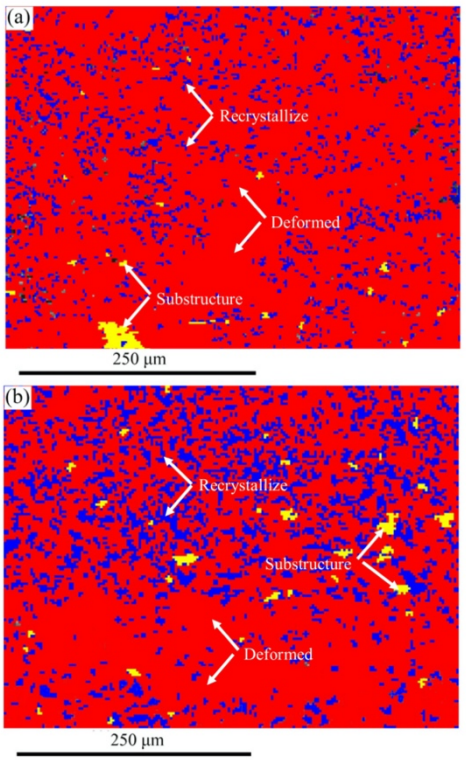

Fig. 14. Types of microstructures in weld seam; (a) high strength and (b) low strength.

In the MOS data, HAGB were defined as being >15° and a comparison between the high and low strength samples. For the majority of LAGB, the MOS was below 10º. However, HAGB has a MOS greater than 10º. In this work, the structure shows characteristics of LAGB which increases as a few recrystallized and the deformed regions increases. The findings are consistent with Acar and Fitzpatrick [27], documented that when welding steel the proportion of LAGB was seen to increase as the degree of plastic deformation was increased. The structure shows that the HAGB value under low strength sample condition was larger than that of the high strength, due to more recrystallized grain. In addition, more recrystallized grain exhibits low grain orientation spread, which caused their strength degradation, consistent with Wang et al. [28], for the grade 91 steel by GTAW method. The residual strain distributions in specimens were evaluated

using kernel average misorientation (KAM). The higher KAM volumes (green color) were higher residual strain. The strain of the high strength and low strength samples is illustrated in Fig. 15.

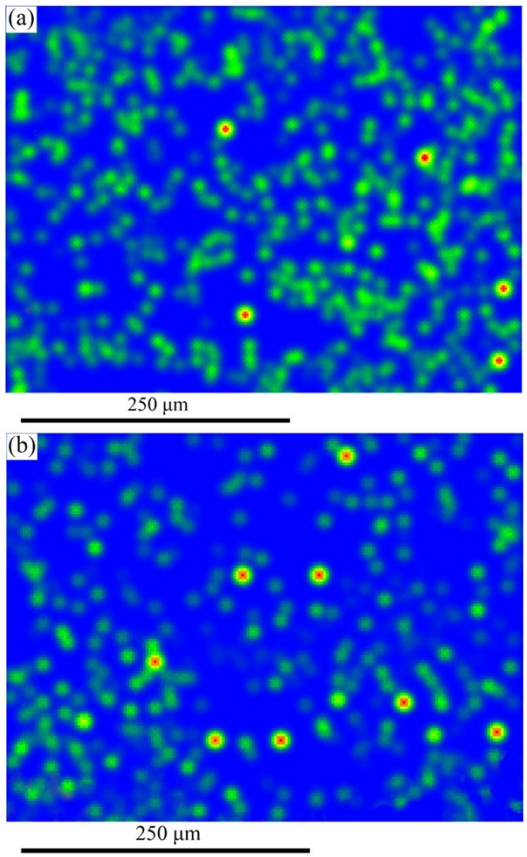

Fig. 15. Residual strain in weld seam; (a) high strength and (b) low strength.

By comparison, higher residual strain was observed under the high strength condition, compared to the low strength condition. Under larger and elongated grain, it may not be able to relax the applied strain on the crystal lattice which remains strained. Greater recrystallized grain contributes to hinder LAGB and reduce residual strain. It is thus possible to conclude that the larger deformation and residual strain with low-angle grain boundaries in the structure plays a significant role in the improved tensile strength of weld seam with low voltage condition in CMT processes.

4. Conclusion

Influences of CMT conditions on microstructure, tensile strength and crystallographic orientation of steel were investigated. Results show that the complex surface of weld seam and minimal spatter was found at the travel speed of 50 mm/min. However, a small degree of porosity and the best dilution of the bead also occurred with 12 V, 50 mm/min condition. The optimal tensile strength of weld seam was found for 12 V, 50 mm/min condition. For optimal tensile strength, the strong preferred orientation of the elements and intermetallic phase formed on the {100} plane. Only the ferrite phase with a BCC crystal structure was present in the weld seam. The larger tensile strength with more deformed, a few recrystallization structures was positively correlated to the low-angle grain boundaries behavior, and residual strain in microstructure.

Acknowledgements

This work was financially supported by the National Research Council of Thailand, Grant numbers A-6/2561. The authors would like to thank the Rajamangala University of Technology Rattanakosin.

References

[1] Liang SF, Chi LX, Gao XZ, Yan BL. Process parameters and mechanical properties of SAPH440 steel in pulse arc welding with different heat inputs. IOP Conference Series: Materials Science and Engineering 2020;770:012104.

[2] Kim C, Choi J, Kang M, Park Y. A study on the CO_2 laser welding characteristics of high strength steel up to 1500 MPa for automotive application. J Achiev Mater Manuf Eng 2010;39: 79-86.

[3] Jahandideh AR, Hamedi M, Mansourzadeh SA, Rahi A. An experimental study on effects of postheating parameters on resistance spot welding of SAPH440 steel. Sci Technol Weld Join 2011;16: 669-75.

[4] Çelebi A. Deformation and Microstructural Analysis of Fiber Laser and TIG Welding of Thin Ti6Al4V Sheet by Coordinate Measurement Machine (CMM). Politeknik Dergisi 2020;23: 1183-8.

[5] Boumerzoug Z, Derfouf C, Baudin T. Effect of Welding on Microstructure and Mechanical Properties of an Industrial Low Carbon Steel. Eng 2010;02: 502-6.

[6] Alipooramirabad H, Paradowska A, Ghomashchi R, Reid M. Investigating the effects of welding process on residual stresses, microstructure and mechanical properties in HSLA steel welds. J Manuf Process 2017;28: 70-81.

[7] Ikpe AE, Ikechukwu O, Ikpe E. Effects of Arc Voltage and Welding Current on the Arc Length of Tungsten Inert Gas Welding (TIG). Int J Eng Technol 2017;3: 213-21.

[8] Zhao Y, Shi X, Yan K, Wang G, Jia Z, He Y. Effect of shielding gas on the metal transfer and weld morphology in pulsed current MAG welding of carbon steel. J Mater Process Technol 262 2018;262: 382-91.

[9] Mvola B, Kah P, Layus P. Review of current waveform control effects on weld geometry in gas metal arc welding process. Int J Adv Manuf Technol 2018:96: 4243-65.

[10] Selvi S, Vishvaksenan A, Rajasekar E. Cold metal transfer (CMT) technology - An overview. Def Technol 2018;14: 28-44.

[11] Rajeev GP, Kamaraj M, Bakshi SR. Effect of correction parameters on deposition characteristics in cold metal transfer welding. Mater Manuf Process 2019;34: 1205-16.

[12] Zhu ZY, Liu YL, Gou GQ, Gao W, Chen J. Effect of heat input on interfacial characterization of the butter joint of hot-rolling CP-Ti/Q235 bimetallic sheets by Laser + CMT. Sci Rep 2021;11: 1-11.

[13] Koli Y, Yuvaraj N, Vipin, Aravindan S. Investigations on weld bead geometry and microstructure in CMT, MIG pulse synergic and MIG welding of AA6061-T6. Mater Res Express 2019;6(12): 1-25.

[14] Azar AS, Svensson LE, Nyhus B. Effect of crystal orientation and texture on fatigue crack evolution in high strength steel welds. Int J Fatigue 2015;77: 95-104.

[15] Tang X, Zhang S, Cui X, Zhang C, Liu Y, Zhang J. Tribological and cavitation erosion behaviors of nickel-based and iron-based coatings deposited on AISI 304 stainless steel by cold metal transfer. J Mater Res Technol 2020;9: 6665-81.

[16] Nikam PP, Arun D, Ramkumar KD, Sivashanmugam N. Microstructure characterization and tensile properties of CMT-based wire plus arc additive manufactured ER2594. Mater Charact 2020;169: 110671.

[17] Chen T, Xue S, Wang B, Zhai P, Long W. Study on short-circuiting GMAW pool behavior and microstructure of the weld with different waveform control methods. Metals 2019;9: 1326.

[18] Lin W, Yiming M, Jie X, Ji C. Improving spreadability of molten metal in MIG welding-brazing of aluminum to steel by external magnetic field. J Manuf Process 2022;81: 35-47.

[19] Wagiman A, Bin Wahab MS, Mohid Z, Mamat A. Effect of GMAW-CMT heat input on weld bead profile geometry for freeform fabrication of aluminium parts. Appl Mech Mater 2014;465-466: 1370-4.

[20] Iván T, Paskual A, Álvarez P, Suárez A. Study on Arc Welding Processes for High Deposition Rate Additive Manufacturing. Procedia CIRP 2018;68:358-62.

[21] Pickin CG, Young K. Evaluation of cold metal transfer (CMT) process for welding aluminium alloy. Sci Technol Weld Join 2006;11: 583-5.

[22] Deepak J.R, Jeevahan J.J, Ramachandran D, Sai Suhas S.V, Praneethkumar Reddy P.V. XRD investigation of GTAW, GMAW, LBW and AGTAW Corten A588 grade steel weldments. Materials Today: Proceedings 2021;47(14): 4844-51.

[23] Oshida Y. Magnesium Materials: From Mountain Bikes to Degradable Bone Grafts, Berlin, Boston: De Gruyter; 2021.

[24] Yu L, Nakata K, Yamamoto N, Liao J. Texture and its effect on mechanical properties in fiber laser weld of a fine-grained Mg alloy. Mater Lett 2009;63: 870-2.

[25] Ifergane S, Barkay Z, Beeri O, Eliaz N. Study of fracture evolution in copper sheets by in situ tensile test and EBSD analysis. J Mater Sci 2010;45: 6345-52.

[26] Sarkari Khorrami M, Saito N, Miyashita Y. Texture and strain-induced abnormal grain growth in cryogenic friction stir processing of severely deformed aluminum alloy. Mater Charact 2019;151: 378-89.

[27] Acar MO, Fitzpatrick ME. Determination of plasticity following deformation and welding of austenitic stainless steel. Mater Sci Eng A 2017;701: 203-13.

[28] Wang Y, Zhang W, Wang Y, Lim YC, Yu X, Feng Z. Experimental evaluation of localized creep deformation in grade 91 steel weldments. Mater Sci Eng A 2021;799: 140356.